CAMBRIDGE
UNIVERSITY PRESS

Article

Grandviewite redefinition, new formula Cu$_3$Al$_2$(SO$_4$)(OH)$_{10}$·H$_2$O, and crystal-structure determination

Jiří Sejkora[1]* , Gwladys Steciuk[2], Maria Florencia Marquez-Zavalia[3,4], Jakub Plášil[2] and Zdeněk Dolníček[1]

[1]Department of Mineralogy and Petrology, National Museum, Cirkusová 1740, CZ-193 00 Prague 9, Czech Republic; [2]Institute of Physics ASCR, v.v.i., Na Slovance 2, CZ-182 21 Prague 8, Czech Republic; [3]Dpto. de Mineralogía, Petrografía y Geoquímica, IANIGLA-CONICET-CCT MENDOZA, Avda. A. Ruiz Leal s/n Parque General San Martín, C.C. 330 (5500) Mendoza, Argentina and [4]Mineralogía y Petrología, FAD, Universidad Nacional de Cuyo, Centro Universitario, 5502, Mendoza, Argentina

Abstract

Grandviewite is redefined on the basis of a reinvestigation of the holotype specimen from the Grandview mine, Arizona, USA, and additional specimens found in the Restauradora vein at the Capillitas mine, northwestern Argentina. Grandviewite from the Capillitas mine forms globular masses up to a couple of millimetres in diameter, formed by very thin platy to acicular lath-like crystals, greenish-pale blue in colour, pleochroic (*X* = colourless, *Y* = very pale blue and *Z* = greenish-pale blue), with pale blue streak and silky to a satiny lustre. Results of an electron-microprobe study and crystal-structure determination lead to the new ideal formula Cu$_3$Al$_2$(SO$_4$)(OH)$_{10}$·H$_2$O, which requires (in wt.%) CuO 45.13, Al$_2$O$_3$ 19.28, SO$_3$ 15.14, and H$_2$O 20.45, total 100.00. Its empirical formulas are (Cu$_{2.96}$Mn$_{0.01}$)$_{\Sigma 2.97}$Al$_{2.03}$(SO$_4$)$_{0.97}$(SiO$_4$)$_{0.03}$(AsO$_4$)$_{0.01}$(OH)$_{9.97}$Cl$_{0.01}$·H$_2$O (Grandview mine) and Cu$_{2.97}$(Al$_{2.03}$Fe$_{0.01}$)$_{\Sigma 2.04}$(SO$_4$)$_{0.95}$(SiO$_4$)$_{0.03}$(AsO$_4$)$_{0.01}$(PO$_4$)$_{0.01}$(OH)$_{9.97}$Cl$_{0.01}$·H$_2$O (Capillitas mine). Grandviewite is triclinic, $P\bar{1}$, with unit-cell parameters refined from powder X-ray diffraction data: *a* = 5.713(2), *b* = 10.1374(8), *c* = 10.9791(9) Å, α = 72.240(6)°, β = 82.79(2)°, γ = 86.07(2)°, *V* = 600.5(3) Å^3 and *Z* = 2 (Grandview mine); and *a* = 5.749(3), *b* = 10.1388(13), *c* = 10.9656(16) Å, α = 72.344(1)°, β = 82.83(4)°, γ = 86.77(3)°, *V* = 604.2(3) Å^3 and *Z* = 2 (Capillitas mine). The crystal structure of grandviewite from the Capillitas mine was solved by 3-dimensional electron diffraction analysis (*R*(obs)/*wR*(obs) = 0.1304/0.1316 for 6401/31007 observed reflections with *I* ≥ 3σ(*I*). Grandviewite contains infinite AlO$_6$–Cu1–AlO$_6$ slabs along **a** connected on both ends to Cu2 [4 + 1]–SO$_4$ chains. The SO$_4$ tetrahedra form a disordered chain along **a** connected to the Cu2 pyramids on one side and are otherwise stabilised by strong hydrogen bonds to surrounding units. The Raman and infrared spectra for samples from both occurrences are identical. The redefinition (new chemical formula and triclinic symmetry) has been approved by the Commission on New Minerals, Nomenclature and Classification of the International Mineralogical Association (number 21-K).

Introduction

Grandviewite was described by Colchester *et al.* (2008) from the Grandview mine, Arizona, USA. This mineral was found as rare greenish-blue radiating sprays of extremely acicular laths occurring in goethite-rich gossan, in association with chalcoalumite, cyanotrichite and carbonatecyanotrichite. Its chemical formula based on atomic absorption spectrometry, colorimetry, and thermogravimetric analyses was given as Cu$_3$Al$_9$(SO$_4$)$_2$(OH)$_{29}$. Due to the quality of available material and crystals only 2 μm thick, the crystal structure could not be determined at that time. Possible unit-cell parameters were found by auto-indexing of powder X-ray diffraction (PXRD) data and refinement in a monoclinic setting, with *a* = 10.908(2), *b* = 6.393(3), *c* = 10.118(2) Å, β = 107.47° and *V* = 673.0(1) Å^3. Possible space groups suggested by Colchester *et al.* (2008) are *P*2, *P*2$_1$, *Pm*, *P*2/*m*, or *P*2$_1$/*m*.

A similar greenish-blue mineral was found by one of the authors (MFMZ) during a fieldtrip in 1982 in the Restauradora vein at Capillitas mine, northwestern Argentina. On the basis of incomplete analytical data, this mineral was considered as a cyanotrichite-like mineral, related to cyanotrichite and carbonatecyanotrichite (Márquez-Zavalía and Pedregosa, 1994). Later, we restudied this material and found the powder X-ray diffraction data to be identical with that published for grandviewite by Colchester *et al.* (2008). Nevertheless, its chemical composition was significantly different from the published one for grandviewite from the type locality (Colchester *et al.*, 2008). For these reasons, we have decided to reinvestigate the mineral grandviewite. A small part of the holotype sample of grandviewite (M50490) for our study was kindly provided from the collections of Museum Victoria, Melbourne, Australia, by Stuart J. Mills and Oskar Lindenmayer. Our reinvestigation resulted in redefinition with new chemical formula, triclinic symmetry, and determination of its crystal structure. Details of this research are presented in this paper.

This redefinition was approved by the Commission on New Minerals, Nomenclature and Classification (CNMNC) of the International Mineralogical Association (IMA) (proposal 21-K, Miyawaki *et al.*, 2022). The grandviewite samples from the
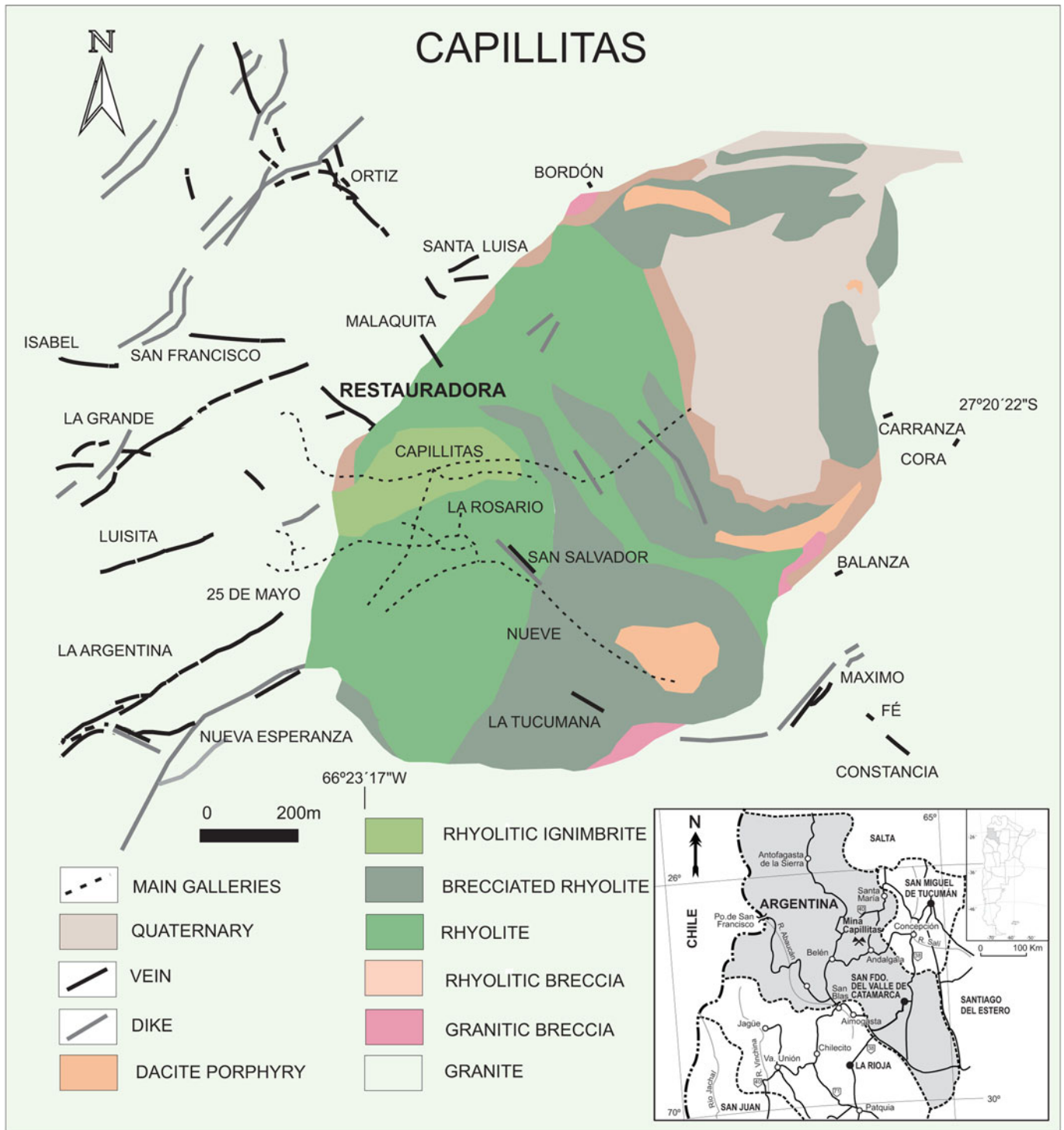
Fig. 1. Schematic geology of Capillitas, showing the location of the Restauradora vein (modified from Márquez-Zavalía *et al.*, 2020).

Capillitas mine studied are deposited in the collections of the Department of Mineralogy and Petrology of the National Museum, Prague, Czech Republic, under the catalogue number P1P 2/2022.

Occurrence and mineral description

Occurrence in Argentina

Grandviewite occurs in the Restauradora vein of the Capillitas mine, which mines an epithermal precious- and base-metal vein

deposit, located along the eastern slope of the Capillitas Range, in Catamarca province, northwestern Argentina (Fig. 1). The volcanism from which the mineralisation of the Capillitas mine and the other genetically linked deposits of the region (e.g. Farallón Negro, Alto de la Blenda, La Alumbrera, Agua Tapada, Cerro Atajo, Agua Rica) are derived (Marquez-Zavalía and Heinrich, 2016 and references therein), developed in a back-arc position of the Miocene–Recent volcanic arc, along the Carachipamapa–Farallón Negro transversal volcanic chain of the Central Andes,

Fig. 2. Globular aggregates of grandviewite from Capillitas mine, Argentina, specimen number P1P 2/2022. The field of view = 1.8 mm, photo J. Sejkora.

Table 2. Chemical composition of grandviewite.

	Grandview mine, Arizona*			Capillitas mine, Argentina			Ideal[a]	Original[b]
	mean	range	S.D.	mean	range	S.D.		
CuO	42.33	40.61–44.72	1.47	42.09	40.38–46.26	1.56	45.13	21.4
ZnO	0.03	0.00–0.14	0.05	0.03	0.00–0.21	0.06		
MnO	0.07	0.00–0.16	0.05	0.05	0.00–0.36	0.09		
Al_2O_3	18.61	16.89–20.22	0.90	18.49	16.87–20.15	0.88	19.28	40.7
Fe_2O_3	0.06	0.00–0.10	0.03	0.14	0.00–0.32	0.08		
SiO_2	0.27	0.00–0.49	0.19	0.37	0.00–1.02	0.27		
As_2O_5	0.11	0.00–0.78	0.24	0.25	0.00–1.12	0.30		
P_2O_5	0.04	0.00–0.20	0.07	0.07	0.00–0.35	0.11		
SO_3	14.00	13.07–14.06	0.45	13.60	12.94–14.52	0.37	15.14	14.5
Cl	0.05	0.00–0.10	0.03	0.06	0.00–0.16	0.05		
H_2O[c]	19.38			19.23			20.45	23.3
–O = Cl	0.02			0.02				
Total	94.94			94.37			100.00	99.9

* Part of holotype M50490 (Museums Victoria, Melbourne, Australia)
a – ideal composition; b – data published for holotype sample from Grandview mine by Colchester *et al.* (2008); c – H_2O contents calculated by valence balance and stoichiometry of ideal formula $Cu_3Al_2(SO_4)(OH)_{10} \cdot H_2O$.

and has dominant high-K calc-alkaline to shoshonitic affinities (Viramonte *et al.*, 1984). The lithology comprises the upper Precambrian to lower Cambrian folded pelites of the Suncho Formation and the Buey Muerto mica schists, both intruded by the late orogenic Capillitas granite in the Ordovician to the Lower Silurian during the Famatinian Orogenic Cycle. The NE-striking structural fabrics in the Neoproterozoic – early Cambrian Pampean basement were reactivated, forming a tilt-block province. The Capillitas granite is overlain unconformably by the El Morterito Formation and the Farallón Negro Volcanic Complex Cenozoic units, and by undifferentiated Quaternary deposits.

In the Capillitas area, the rocks of the Farallón Negro Volcanic Complex form an ellipsoidal diatreme (1500 m × 900 m), with the long axis striking NE; hydrothermal alteration is widespread, varying laterally by host-rock type. Twenty veins are hosted by the volcanic and granitic rocks in ENE and WNW directions (Márquez-Zavalía, 1999) and the mineralisation is very diverse with more than 120 minerals among primary and secondary species described by several authors (e.g. Márquez-Zavalía *et al.*, 1999, 2020; Márquez-Zavalía and Craig, 2004; Márquez-Zavalía, 2006; Putz *et al.*, 2009). It is the type locality for five minerals: putzite (Paar *et al.*, 2004), catamarcaite (Putz *et al.*, 2006), ishiharaite (Márquez-Zavalía *et al.*, 2014), lislkirchnerite (Effenberger *et al.*, 2015) and omariniite (Bindi *et al.*, 2017).

The deposit has been discontinuously mined for gold since pre-Colombian times. Extensive work was carried out over the last two centuries, interspersed with sporadic copper recovery attempts that were interrupted by metallurgical problems, mainly due to the lack of detailed knowledge of the mineralogy of the ore to be treated. Since the second part of the last century, mining has been mostly restricted to the extraction of banded – and

sporadically stalactitic – rhodochrosite, the main gangue mineral in some of the veins, and for which the Capillitas mine is known worldwide.

Grandviewite was found in samples from the Restauradora vein dumps (27°20'22"S, 66°23'17"W, 3190 m a.s.l.). This vein is hosted by granite, has an average thickness of 50 cm and a total measured length of 106 m. The vein has two branches with strike and dip N10°W / N70°E and 75°E–75°W / 70°S, respectively. The works performed along this vein consist of a 100 m gallery, two inclines, and a shaft. There are two dumps, one at the gallery level and the other below it, formed from the droppings of the one above; most of the material is oxidised. The main hypogene minerals are: pyrite, sphalerite, galena, chalcopyrite, tennantite-(Zn) and tennantite-(Fe), with enargite, hübnerite, gold, stannite, stannoidite, mawsonite, silver and tellurium-bearing minerals as accessory minerals, in a gangue represented principally by quartz; grandviewite is intimately associated with carbonatecyanotrichite and azurite, with antlerite, linarite, malachite and gypsum.

Physical and optical properties

Grandviewite occurs mainly in the cracks or fissures of the host rock, developing globular masses up to a couple of millimetres in diameter, formed by very thin (up to 1 μm) platy to acicular lath-like crystals (Fig. 2), greenish-pale blue in colour, pleochroic (X = colourless, Y = very pale blue and Z = greenish-pale blue), pale blue streak, and silky to satin lustre. In Table 1, its optical data are compared with that published for the holotype from Grandview mine.

Chemical composition

Samples of grandviewite were analysed with a Cameca SX-100 electron microprobe (National Museum, Prague) operating in the wavelength-dispersive mode with an accelerating voltage of 15 kV, a specimen current of 5 nA and a beam diameter of 10 μm. The following lines and standards were used: *K*α: celestine (S), halite (Cl), hematite (Fe), ZnO (Zn), rhodonite (Mn),

Table 1. Summary of optical data for grandviewite.

	Capillitas mine, Argentina Márquez-Zavalía and Pedregosa (1994)	Grandview mine, Arizona Colchester *et al.* (2008)
	biaxial (+)	biaxial (–)
α	1.605(3)	1.590(4)
β	1.626(3)	1.625(4)
γ	1.655(3)	1.645(4)
$2V_{calc}$	82°	72(3)°

Table 3. Powder X-ray diffraction data of grandviewite.

Capillitas mine, Argentina			Grandview mine, Arizona*					Colchester et al. (2008)	
I_{obs}	d_{obs}	d_{calc}	I_{obs}	d_{obs}	d_{calc}	I_{calc}**	h k l	d_{obs}	I_{obs}
0.6	10.386	10.382	1.2	10.393	10.392	2.1	001	10.392	6
56.4	9.671	9.659	28.8	9.653	9.649	49.6	010	9.667	33
0.2	8.441	8.442				0.3	011		
89.6	6.210	6.207	100.0	6.205	6.205	100.0	0$\bar{1}$1	6.208	100
4.4	5.281	5.278	15.0	5.282	5.283	40.7	012	5.287	35
1.8	4.989	4.985, 4.986	1.5	4.983	4.983, 4.983	2.0, 6.2	111, 021	4.992	5
4.9	4.832	4.830	3.6	4.825	4.825	5.3	020	4.828	6
0.3	4.219	4.221	0.6	4.220	4.222	0.9	022	4.225	5
0.9	4.088	4.089	1.0	4.091	4.093	3.3	$\bar{1}$11	4.092	5
100.0	3.949	3.950	78.3	3.947	3.948	76.9	0$\bar{2}$1	3.949	79
0.7	3.619	3.620	3.1	3.623	3.624	6.6	013	3.625	10
0.2	3.463	3.461	0.9	3.466	3.464	3.5	003	3.467	5
7.2	3.374	3.374	4.1	3.371	3.371	11.9	031		
0.9	3.323	3.323	1.9	3.325	3.325	4.0	023	3.332	7
0.6	3.220	3.220	0.4	3.217	3.216	0.8	030		
1.2	3.199	3.198	1.0	3.196	3.197	3.5	032	3.193	6
2.4	3.104	3.103	3.2	3.102	3.102	3.9	0$\bar{2}$2	3.104	6
1.4	2.987	2.987	4.4	2.988	2.988	8.3	0$\bar{1}$3	2.990	9
3.5	2.815	2.814	5.8	2.815	2.815	23.3	033	2.816	14
0.2	2.718	2.719	1.0	2.721	2.722	4.9	014	2.721	8
1.1	2.524	2.525	0.5	2.523	2.522	2.2	041	2.522	4
3.1	2.4930	2.4932	2.2	2.4914	2.4915	6.9	042	2.493	6
8.8	2.4153	2.4148	5.0	2.4121	2.4123	11.3	040	2.413	9
0.8	2.3866	2.3878				22.0	$\bar{2}$02		
1.7	2.3341	2.3350	7.1	2.3345	2.3345	7.5	043	2.336	5
								2.208	3
0.3	2.0758	2.0764	0.8	2.0783	2.0785	2.3	005	2.076	5
5.5	2.0189	2.0186	3.2	2.0169	2.0170	19.0	052	2.019	8
1.0	1.9750	1.9741	0.9	1.9737	1.9736	8.0	$\bar{2}$1$\bar{3}$	1.974	4
0.3	1.9310	1.9319				0.2	050		
1.1	1.8051	1.8047	0.6	1.8027	1.8030	2.5	0$\bar{5}$1	1.805	5
0.2	1.7771	1.7776	0.4	1.7772	1.7775	1.0	0$\bar{3}$4	1.776	3
0.5	1.7498	1.7499	0.6	1.7490	1.7491	1.5	0$\bar{4}$3	1.750	3
0.9	1.6686	1.6682	0.4	1.6669	1.6665	3.3	061	1.668	4
0.5	1.6214	1.6211	0.9	1.6228	1.6224	5.4	0$\bar{1}$6	1.622	6
0.1	1.6139	1.6142	0.4	1.6192	1.6192	7.1	250		

* Part of holotype M50490 (Museums Victoria, Melbourne, Australia);
** I_{calc} – intensities calculated using the software *PowderCell*2.3 (Kraus and Nolze, 1996) on the basis of the crystal-structure data given in the crystallographic information file.

chalcopyrite (Cu), sanidine (Al, Si) and fluorapatite (P); and Lα: clinoclase (As). Peak counting times (CT) were 20 s and CT for each background was one-half of the peak time. The raw intensities were converted to concentrations automatically using the *PAP* (Pouchou and Pichoir, 1985) matrix-correction procedure. The contents of Ba, Bi, Ca, Co, F, K, Mg, N, Na, Ni, Pb, Sb, Sr,

Th, U, V and Y were sought but found to be below the detection limit (∼0.05–0.20 wt.%). Water content could not be analysed directly because of the minute amount of material available. The H_2O content was confirmed by Raman and infrared spectroscopy and calculated by valence balance and stoichiometry of the ideal formula from the crystal-structure refinement. Lower totals after adding the calculated water contents and a wide range of analytical totals of both studied samples reflect (1) partial dehydration of samples in the vacuum of the electron microprobe chamber or under the electron beam and (2) the thin acicular nature of grandviewite.

The chemical composition of both grandviewite samples studied (Table 2) is very similar and agrees well with the ideal formula $Cu_3Al_2(SO_4)(OH)_{10} \cdot H_2O$ derived from the crystal-structure refinement of 3D electron diffraction data. Their empirical formulae based on 16 anions are the following: $(Cu_{2.96}Mn_{0.01})_{\Sigma 2.97}Al_{2.03}(SO_4)_{0.97}(SiO_4)_{0.03}(AsO_4)_{0.01}(OH)_{9.97}Cl_{0.01} \cdot H_2O$ (Grandview mine – mean of nine analyses) and $Cu_{2.97}(Al_{2.03}Fe_{0.01})_{\Sigma 2.04}(SO_4)_{0.95}(SiO_4)_{0.03}(AsO_4)_{0.01}(PO_4)_{0.01}(OH)_{9.97}Cl_{0.01} \cdot H_2O$ (Capillitas mine – mean of 23 analyses).

Our results differ significantly from data published for grandviewite (Table 2) in the original publication of Colchester *et al.* (2008) based on analyses of hand-picked bulk samples by the

Table 4. Unit-cell parameters of grandviewite (triclinic, space group $P\bar{1}$) refined from PXRD.*

	Capillitas mine, Argentina	Grandview mine, Arizona
a (Å)	5.749(3)	5.713(2)
b (Å)	10.1388(13)	10.1374(8)
c (Å)	10.9656(16)	10.9791(9)
α (°)	72.344(1)	72.240(6)
β (°)	82.83(4)	82.79(2)
γ (°)	86.77(3)	86.07(2)
V (Å)	604.2(3)	600.5(3)
$a:b:c$	0.5670:1:1.0815	0.5636:1:1.0830
Z	2	2
d_{ideal} (g.cm^{-3})	2.906	2.924
$d_{empirical}$ (g.cm^{-3})	2.904	2.921

* d_{ideal}, $d_{empirical}$ – calculated for ideal and empirical formula, respectively.

Table 5. Raman and infrared spectra of grandviewite.*

Raman				Infrared				Assignment
Capillitas		Grandview		Capillitas		Grandview		
3518	w	3511	w	3563	ms	3562	ms	ν(OH) stretching vibrations of (OH) groups and hydrogen-bonded water molecules
3309	w	3317	w	3310	s	3305	s	
				3197	s	3181	s	
				2920	ms	2914	ms	
				1628	ms	1633	ms	$\nu_2(\delta)$ hydrogen-bonded water molecules
1197	w	1195	w	1159	m	1158	m	$\nu_3(SO_4)^{2-}$ antisymmetric stretching vibrations
				1109	vs	1104	vs	
1073	w	1074	w	1060	vs	1058	vs	
974	vs	970	vs	973	ms	970	ms	$\nu_1(SO_4)^{2-}$ symmetric stretching vibrations
				909	ms	912	ms	
				775	ms	771	ms	Libration modes of H_2O molecules
668	w	664	w	667	ms	665	ms	$\nu_4(\delta)(SO_4)^{2-}$ bending vibrations
611	w	611	w	614	w	617	w	
				593	w	592	w	
534	s	533	s					Vibrations of Cu–O and Al–O bonds
485	w	490	w	505	s	570	s	$\nu_2(\delta)(SO_4)^{2-}$ bending vibrations
446	w	443	w	450	s	451	s	
417	w	415	w	422	s	419	s	
329	w	332	w					Libration modes of H_2O molecules, vibrations of Cu–O and Al–O bonds, and lattice modes
271	ms	270	ms					
213	w	208	w					
123	ms	118	ms					
82	ms	77	ms					
65	ms	63	ms					

* Wavenumbers in cm^{-1}; intensity: vs – very strong, s – strong, ms – medium strong, w – weak.
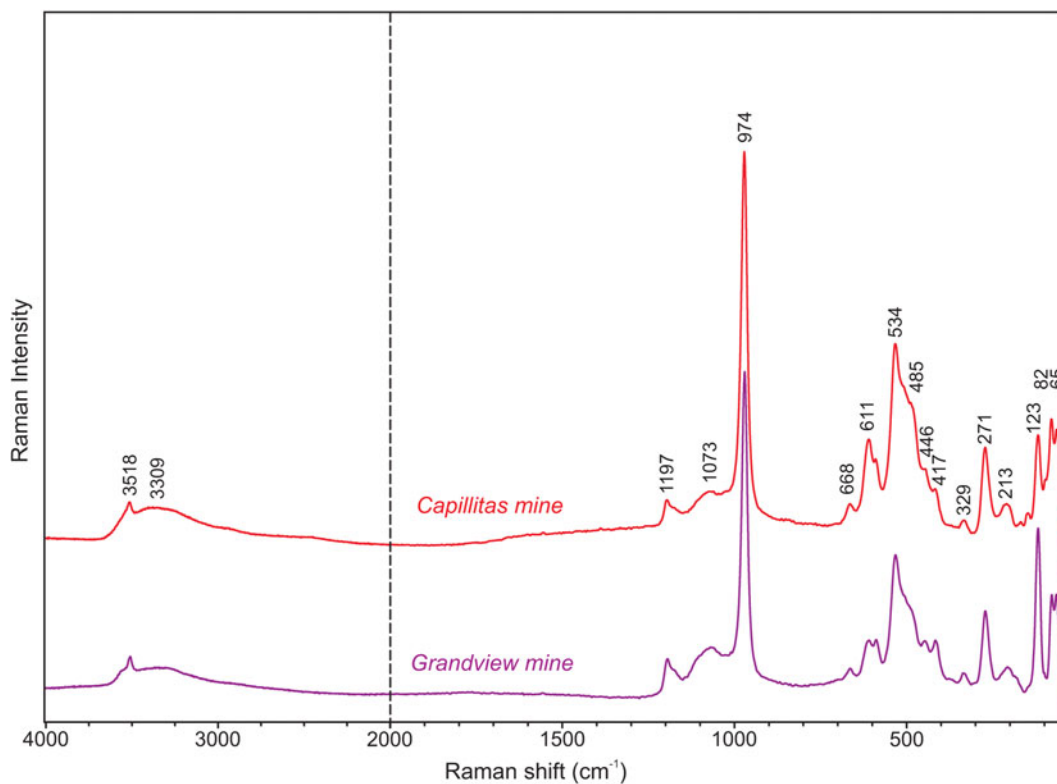

Fig. 3. Raman spectrum of holotype grandviewite (split at 2000 cm^{-1}) from the type locality the Grandview mine, Arizona, in comparison with grandviewite from the Capillitas mine, Argentina.
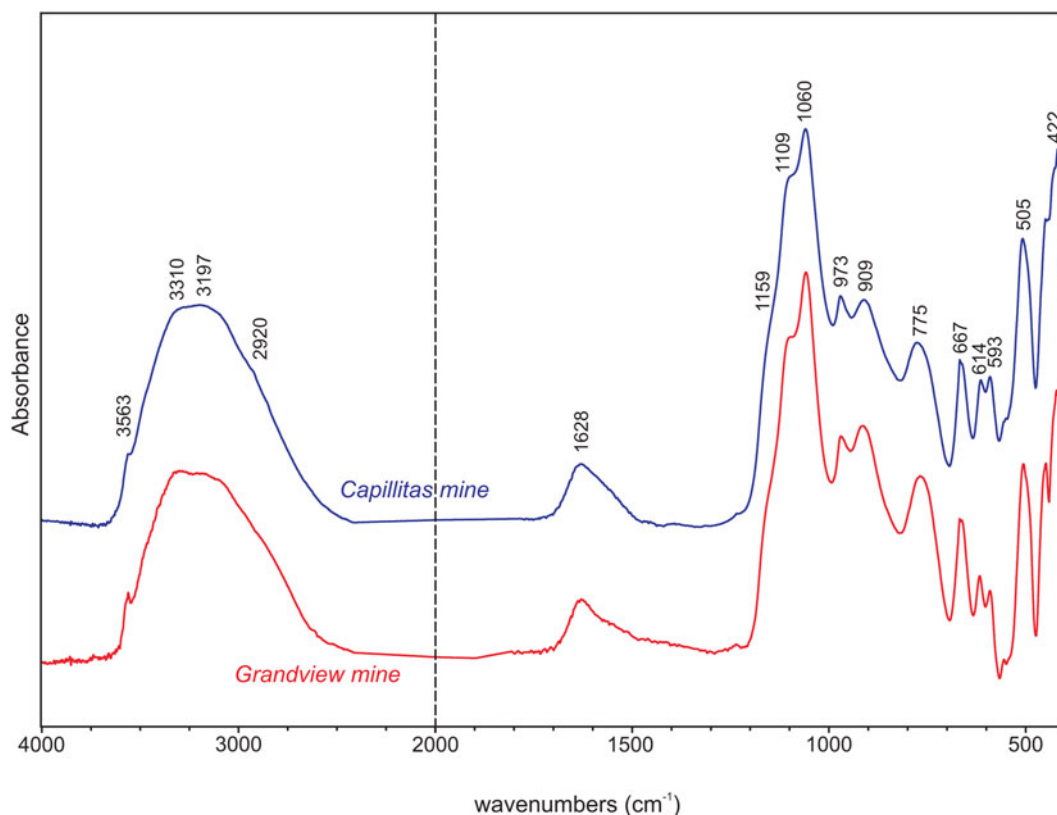
Fig. 4. Infrared spectrum of holotype grandviewite (split at 2000 cm^{-1}) from the type locality Grandview mine, Arizona, in comparison with grandviewite from the Capillitas mine, Argentina.

AAS (Cu), colorimetry (Al) and thermogravimetric analyses (S and H$_2$O). The most likely explanation is that Colchester *et al.* (2008) used an indistinguishable mixture of grandviewite and intimately associated chalcoalumite CuAl$_4$(SO$_4$)(OH)$_{12}$·3H$_2$O, or simply by mistake, confused the values of CuO and Al$_2$O$_3$ contents.

Powder X-ray diffraction data

Powder X-ray diffraction data for both samples were recorded at room temperature using a Bruker D8 Advance diffractometer equipped with a solid-state LynxEye detector and a secondary monochromator producing Cu*K*α radiation housed at the Department of Mineralogy and Petrology, National Museum, Prague, Czech Republic. The instrument was operating at 40 kV and 40 mA. In order to minimise the background, the powder samples were placed on the surface of a flat silicon wafer. The powder pattern was collected in the Bragg–Brentano geometry in the range 3–70°2θ, with a step of 0.01° and a counting time of 20 s per step (total duration of the experiment was ca. 30 hours). The positions and intensities of diffractions were found and refined using the Pearson VII profile-shape function of the *ZDS* program package (Ondruš, 1993). The peak positions in experimental patterns of both samples are very similar and agree very well with data published for grandviewite (Table 3) by Colchester *et al.* (2008); the observed differences in intensity of diffraction are caused by minimal amounts of samples available and preferred orientation effects. The unit-cell parameters refined by the least-squares program of Burnham (1962) for both samples are comparable (Table 4). Only in the case of the *a* parameter was

a small difference (5.749/5.713 Å) found. The observed differences in the unit-cell parameters of grandviewite obtained from the 3D ED data (Table 5) and those from the PXRD data are probably due to the temperature of measurement. The 3D ED data were recorded at 100 K to preserve the hydrated nature of the mineral under TEM vacuum, whereas the PXRD data were measured at the ambient temperature – explaining the higher unit-cell volume.

Raman and infrared spectroscopy

The Raman spectra were collected in the range 4000–40 cm^{-1} using a DXR dispersive Raman Spectrometer (Thermo Scientific) mounted on a confocal Olympus microscope. The Raman signal was excited by an unpolarised red 633 nm He–Ne gas laser and revealed by a CCD detector. The experimental parameters were: 100× objective, 30 s exposure time, 100 exposures, 50 μm slit spectrograph aperture and 2 mW laser power level. The spectra were acquired repeatedly from different grains to obtain a representative spectrum with the best signal-to-noise ratio. In addition, the eventual thermal damage of the measured point was excluded by visual inspection of the excited surface after measurement, by observation of possible decay of spectral features at the start of excitation and by checking for thermal downshift of Raman lines. The instrument was set up by a software-controlled calibration procedure using multiple neon emission lines (wavelength calibration), multiple polystyrene Raman bands (laser frequency calibration), and standardised white-light sources (intensity calibration). Spectral manipulations were performed using *Omnic 9* software (Thermo Scientific).
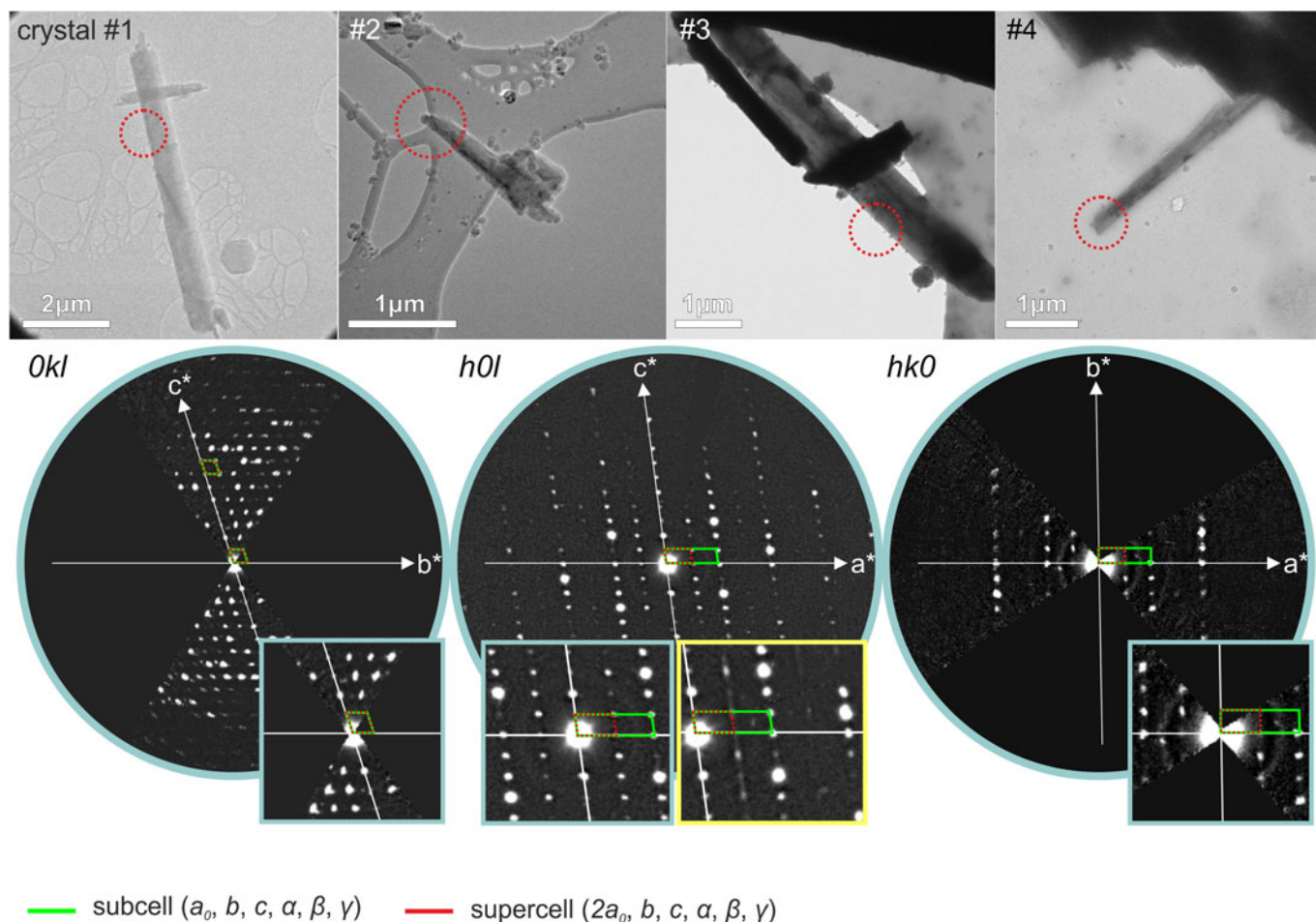
Fig. 5. Four grandviewite crystals used for the 3D ED analysis and sections of the reciprocal space with the two triclinic indexings in the subcell (green) and the supercell (red). The dotted red circles on each crystal represent the area selected and the beam size during data collections.

The infrared vibrational spectra were recorded by the attenuated total reflection (ATR) method with a diamond cell on a Nicolet iS5 spectrometer. Spectra over the 4000–400 cm^{-1} range were obtained by the co-addition of 64 scans with a resolution of 4 cm^{-1} and a mirror velocity of 0.4747 cm/s. Spectra were co-added to improve the signal-to-noise ratio.

The Raman spectra of grandviewite from both localities are very close (Fig. 3). A similar situation was observed for the infrared spectra (Fig. 4). The following interpretation (Table 5) of the spectra is based on the papers of Myneni (2000), Nakamoto (2009), Frost *et al.* (2009) and Čejka *et al.* (2011). Bands of low intensity, located at 3518 and 3309 cm^{-1} (R – Raman) and more prominent bands at 3563, 3310, 3197 and 2920 cm^{-1} (IR – infrared) are connected with the ν(OH) stretching vibrations of (OH) groups and hydrogen-bonded water molecules. A band at 1628 cm^{-1} (IR) is attributed to the $\nu_2(\delta)$ hydrogen-bonded water molecules. The low-intensity bands at 1197 and 1073 cm^{-1} (R) and strong band at 1060 with shoulders at 1109 and 1159 cm^{-1} (IR) are assigned to the split triply degenerate $\nu_3(SO_4)^{2-}$ antisymmetric stretching vibrations. The most intensive band at 974 cm^{-1} (R) and medium-strong bands at 973 and 909 cm^{-1} (IR) are attributed to the $\nu_1(SO_4)^{2-}$ symmetric stretching vibrations. Weak to medium strong bands at 668 and 611 cm^{-1} (R) and 667, 614 and 593 cm^{-1} (IR) are connected with the split triply degenerate $\nu_4(\delta)(SO_4)^{2-}$ bending vibrations. Weak bands at 485,

446 and 417 cm^{-1} (R) and strong bands 505, 450 and 422 cm^{-1} (IR) are assigned to the split doubly degenerate $\nu_2(\delta)(SO_4)^{2-}$ bending vibrations. The other observed bands at 534, 329, 271, 213, 123, 82 and 65 cm^{-1} (R) and 775 cm^{-1} (IR) are probably connected with libration modes of H_2O molecules, vibrations of Cu–O and Al–O bonds, and lattice modes.

Gladstone–Dale compatibility

The Gladstone–Dale compatibility (Mandarino, 1981) 1–(K_P/K_C), calculated from the unit-cell parameters refined from PXRD data, is superior for both occurrences; Grandview mine, Arizona: 0.004 and 0.005 for ideal and empirical formula, respectively; Capillitas mine, Argentina: –0.016 and –0.014 for ideal and empirical formula, respectively.

Crystal structure of grandviewite

3D Electron diffraction analysis

Due to the nature of the crystals (very thin laths), transmission electron microscopy has been chosen to investigate the structural properties of grandviewite from the Capillitas mine.

The 3D electron diffraction (ED) data were collected in an FEI Tecnai 02 transmission electron microscope (TEM) (acceleration

Table 6. Crystallographic parameters from 3D ED at 100 K for grandviewite.

Crystal data

Refined structural formula	$Cu_3Al_2(SO_4)(OH)_{10}(H_2O)$
Crystal system	triclinic
Space group	$P\bar{1}$
a, b, c (Å) *	6.002(3), 10.54(3), 11.249(8)
α, β, γ (°)	72.14(17), 81.56(60), 86.10(79)
V (Å^3)	669.8(12)
Z	2
Density (g·cm^{-3})	2.6117

Data collection

Temperature	100 K
Crystal shape	lath-shaped
TEM	FEI Tecnai 02
Radiation (wavelength)	electrons (0.0251 Å)
Resolution range (sinθ/λ)	0.05–0.755 Å^{-1}
Limiting Miller indices (h, k, l)	−8→9, −14→15, 0→17
No. of collected reflections (obs/all) – kinematic	5088/19982
No. of independent reflections (obs/all) – kinematic	714/4517
R_{int} (obs/all) – kinematic	0.1703/0.3380
Redundancy	4.424
Coverage for sinθ/λ = 0.72 Å^{-1}	94.93%

Dynamical refinement

RSg(max) (for all four crystals)	0.6
No. of reflections (obs/all)	All: 6401/31007
	$h = 2n$: 5648/15688
	$h = 2n + 1$: 754/15319
	(obs: $h = 2n + h = 2n + 1$)
	Crystal 1: 1621 + 90
	Crystal 2: 1036 + 250
	Crystal 3: 1802 + 264
	Crystal 4: 1189 + 150
R(obs)/wR (obs)	All: 0.1304/0.1316
	$h = 2n$: 0.1222/0.1271
	$h = 2n + 1$: 0.2386/0.2404
	Crystal 1: 0.1361/0.1416
	Crystal 2: 0.1186/0.1050
	Crystal 3: 0.1209/0.1279
	Crystal 4: 0.1533/0.1474
N all parameters/N struct. parameters	448/118
Refined thicknesses from crystal 1 to 4	605, 149, 445, 260

* The lattice parameters are averaged from six 3D ED data sets collected on six different crystals.

Table 7. Hydrogen distances (d in Å) from the difference-Fourier map (without refinement) for grandviewite.*

H1Oi	Oi	Oj	d(H–Oi)	d(H–Oj)	σ[ΔV(r)]
H1O1_1	O1_1	O7_2	1.04	2.32	>3σ
H1O1_2	O1_2	O7_1	0.98	1.93	>3σ
H1O2_1	O2_1	O7_2	1.08	1.86	>3σ
H1O2_2	O2_2	O7_1	1.09	1.74	>3σ
H1O3_1	O3_1	O5_2	1.07	1.82	>3σ
H1O3_2	O3_2	O5_1	0.98	1.6	>3σ
H1O4_1	O4_1	O8_1	1	1.72	>4σ
H1O4_2	O4_2	O8b_2	1.02	1.7	>2.5σ
H1O5_1	O5_1	O8b_2	1.08	1.96	>3σ
H1O5_2	O5_2	O8b_1	0.94	1.93	>3σ
		average:	1.03(2)		

* Oi = donor, Oj = acceptor.

voltage of 200 kV, LaB$_6$) equipped with a side-mounted CCD camera Olympus SIS Veleta with a 14bit dynamic range. The sample was crushed in a mortar without solvent and deposited on a Au-grid coated by a thin film of holey amorphous carbon. To preserve the hydrated structure of the mineral under the high vacuum in the TEM, the grid was plunged into liquid nitrogen and transferred to the TEM using a Gatan 626 cryo-transfer holder (Gemmi *et al.*, 2019; Mugnaioli *et al.*, 2020; Steciuk *et al.*, 2021a, 2021b). The PEDT technique was chosen to collect stepwise 3D ED data at 100 K. For each selected crystal area (Fig. 5), a series of non-oriented patterns were collected sequentially by a 1° step on the accessible tilt range of the goniometer (Kolb *et al.*, 2007, 2008; Mugnaioli *et al.*, 2009) automated by the in-house software *RATS*, including the tracking of the crystal following the procedure described by Plana-Ruiz (2018). To reduce the dynamical effects, the 3D ED (Gemmi and Lanza, 2019; Gemmi *et al.*, 2019) was coupled with precession electron diffraction (PED) using the precession device Nanomegas Digistar (Vincent and Midgley, 1994). The precession semi-angle was set to 1°. Low illumination settings were used to minimise the beam-induced damage on the crystals. 3D ED data reduction was performed using the computer program *PETS2* (Palatinus *et al.*,
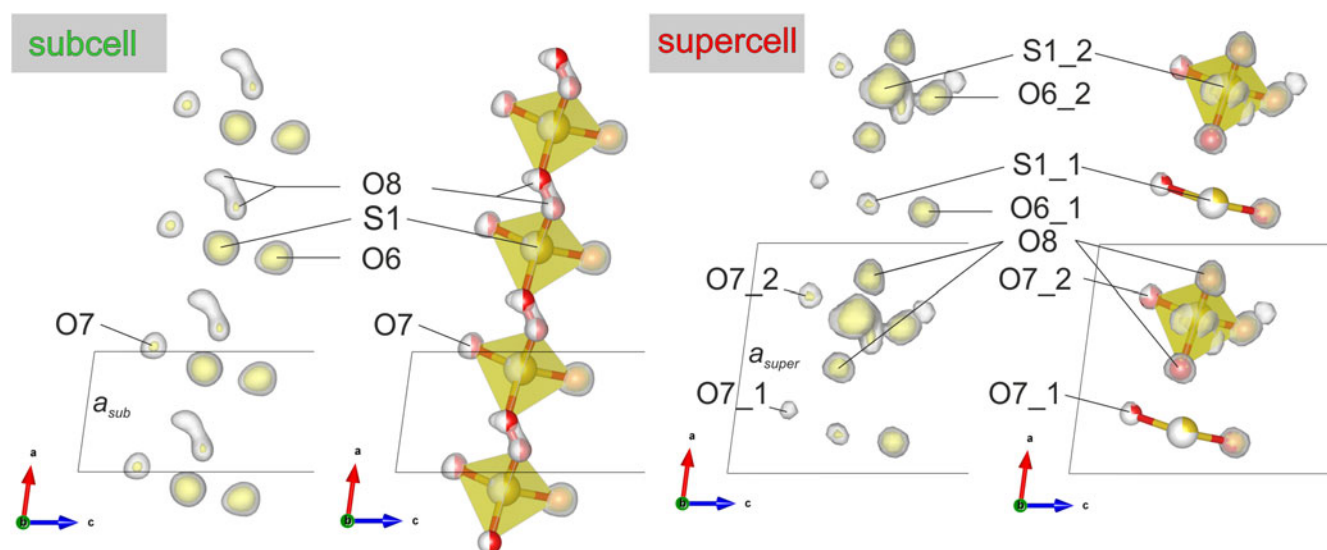

Fig. 6. Visualisation of the SO$_4$ chain in the subcell and in the supercell from the charge-flipping algorithm. In both cases, the electrostatic potential map with isosurface level ≥ 3σ[ΔV(r)] (yellow) and ≥ 2σ[ΔV(r)] (white) and the model are represented.
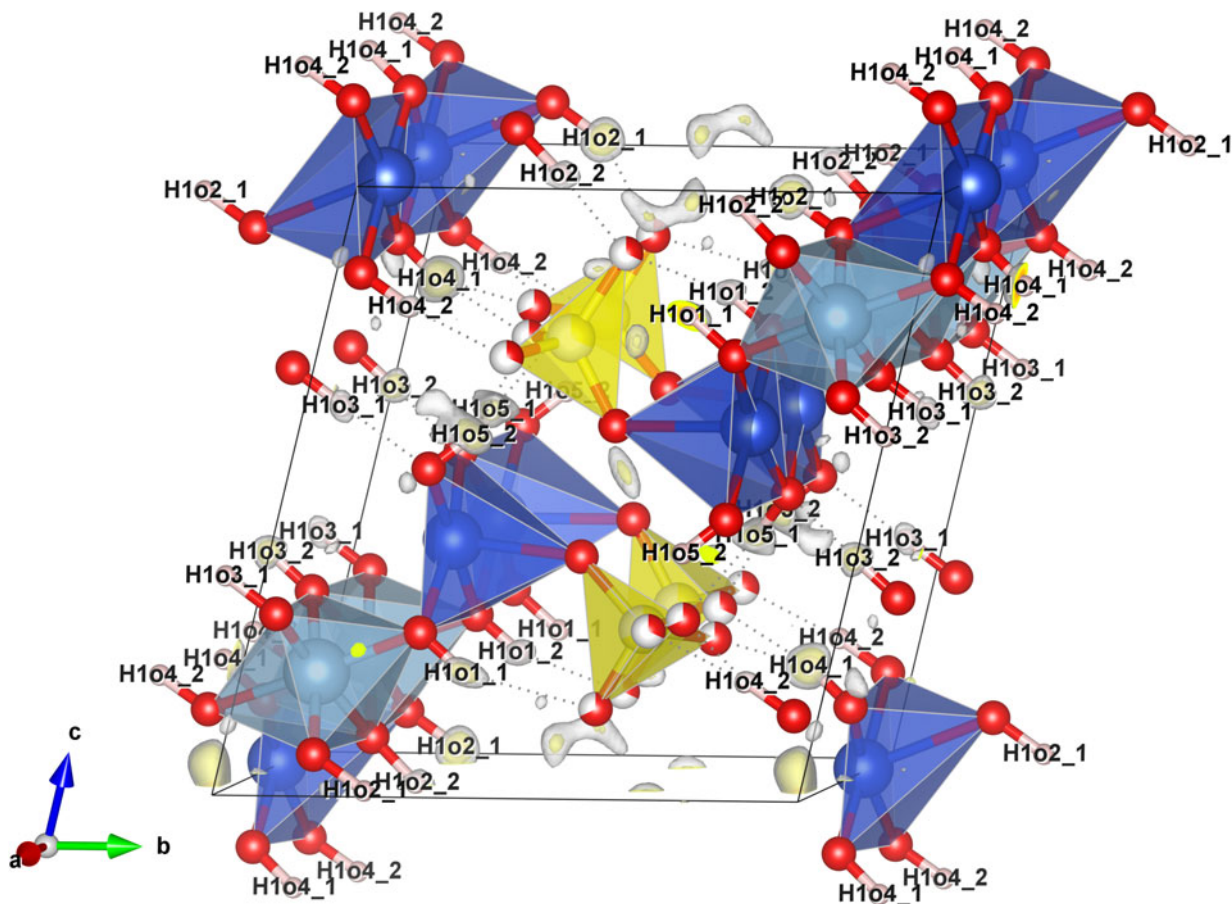
Fig. 7. Determination of the hydrogen sites from the residual electrostatic potential map (equivalent to a difference-Fourier map) in the subcell and in the supercell. The residual map is represented as isosurface with levels $>3\sigma[\Delta V(r)]$ (yellow) and $>2.5\sigma[\Delta V(r)]$ (white). SO_4, AlO_6 and CuO_5 polyhedra are represented in yellow, grey and blue, respectively.

Table 8. Selected interatomic distances (Å) for grandviewite.*

Cu–O		Al–O		S–O		Oi–H1Oi	
Cu1–O2_1	2.483(14)	Al1_1–O1_2	1.986(13)	S1_1–O6_1	1.678(14)	O1_1–H1O1_1	1.055(14)
Cu1–O2_2	2.460(13)	Al1_1–O2_1	2.009(17)	S1_1–O7_1	1.70(2)	O1_2–H1O1_2	1.043(17)
Cu1–O4_1	1.952(14)	Al1_1–O2_2	2.00(2)	S1_1–O8_1	1.80(2)	O2_1–H1O2_1	1.051(13)
Cu1–O4_1	2.016(19)	Al1_1–O3_1	1.97(2)	S1_1–O8_2	1.66(2)	O2_2–H1O2_2	1.039(16)
Cu1–O4_2	2.064(19)	Al1_1–O3_2	1.954(18)	S1_1–O8b_1	1.63(2)	O3_1–H1O3_1	1.030(16)
Cu1–O4_2	2.108(17)	Al1_1–O4_1	2.036(12)	S1_1–O8b_2	2.33(2)	O3_2–H1O3_2	1.023(15)
						O4_1–H1O4_1	1.033(13)
Cu2_1–O1_1	2.071(15)	Al1_2–O1_1	1.973(12)	S1_2–O6_2	1.647(13)	O4_2–H1O4_2	1.032(15)
Cu2_1–O1_2	2.028(19)	Al1_2–O2_1	1.96(2)	S1_2–O7_2	1.622(12)	O5_1–H1O5_1	1.04(3)
Cu2_1–O3_1	2.502(13)	Al1_2–O2_2	2.001(18)	S1_2–O8_1	1.640(17)	O5_2–H1O5_2	1.03(3)
Cu2_1–O5_1	1.945(17)	Al1_2–O3_1	1.961(17)	S1_2–O8_2	2.01(2)		
Cu2_1–O5_2	2.017(19)	Al1_2–O3_2	1.95(2)	S1_2–O8b_1	1.873(18)	Oj–H1Oi	
Cu2_1–O6_1	2.432(17)	Al1_2–O4_2	1.997(12)	S1_2–O8b_2	1.527(16)	O5_1–H1O3_2	1.645(18)
						O5_2–H1O3_1	1.934(19)
Cu2_2–O1_1	2.10(2)					O7_1–H1O1_2	1.96(3)
Cu2_2–O1_2	2.081(16)					O7_1–H1O2_2	1.87(2)
Cu2_2–O5_1	2.00(2)					O7_2–H1O2_1	1.894(17)
Cu2_2–O5_2	2.046(16)					O7_2–H1O1_1	2.28(3)
Cu2_2–O6_2	2.388(17)					O8_1–H1O4_1	1.660(18)
						O8_2–H1O4_2	1.64(2)
						O8B_1–H1O5_2	1.98(3)
						O8B_1–H1O4_1	1.99(2)
						O8B_2–H1O5_1	1.77(4)
						O8B_2–H1O4_2	1.87(2)

* Oi = donor, Oj = acceptor.

Table 9. Site occupation factors (S.o.f.), positional and atomic displacement parameters (in $Å^2$) for grandviewite.

Atom label	S.o.f	x/a	y/b	z/c	U_{iso}
Cu1	1	0.2554(3)	0.9901(3)	0.0025(2)	0.0063(3)
Cu2_1	1	0.1177(3)	0.2528(3)	0.3938(2)	0.0139(2)
Cu2_2	1	0.6079(3)	0.2485(3)	0.3964(2)	0.0139(2)
Al1_1	1	0.4334(4)	0.1245(4)	0.1994(3)	0.0057(3)
Al1_2	1	0.9310(4)	0.1200(4)	0.1989(3)	0.0057(3)
S1_1	0.290(2)	0.1920(15)	0.6043(10)	0.2615(8)	0.0329(8)
S1_2	0.710(2)	0.6722(6)	0.6210(6)	0.2559(4)	0.0329(8)
O1_1	1	−0.1024(7)	0.2759(7)	0.2627(5)	0.0198(5)
O1_2	1	0.3918(7)	0.2836(6)	0.2604(5)	0.0198(5)
O2_1	1	0.2005(6)	0.1873(6)	0.0812(4)	0.0137(5)
O2_2	1	0.7058(6)	0.2018(6)	0.0807(4)	0.0137(5)
O3_1	1	0.1582(6)	0.0544(6)	0.3137(4)	0.0125(5)
O3_2	1	0.6614(6)	0.0416(6)	0.3086(4)	0.0125(5)
O4_1	1	0.4651(7)	0.9699(6)	0.1248(4)	0.0123(5)
O4_2	1	0.9692(8)	0.9630(6)	0.1331(5)	0.0123(5)
O5_1	1	0.3273(7)	0.1909(7)	0.5173(4)	0.0206(6)
O5_2	1	0.8378(6)	0.2135(7)	0.5211(5)	0.0206(6)
O6_1	1	0.1411(8)	0.4810(8)	0.3973(6)	0.0389(9)
O6_2	1	0.6297(9)	0.4808(9)	0.3714(5)	0.0389(9)
O7_1	0.290(2)	0.256(3)	0.5562(16)	0.1296(13)	0.0331(14)
O7_2	0.710(2)	0.7693(10)	0.5774(8)	0.1315(6)	0.0331(14)
O8_1	0.710(2)	0.4367(8)	0.7059(9)	0.2265(7)	0.0230(10)
O8_2	0.290(2)	0.9651(18)	0.7049(17)	0.2507(16)	0.0230(10)
O8b_1	0.290(2)	0.3830(15)	0.6938(13)	0.2840(12)	0.0230(10)
O8b_2	0.710(2)	0.8392(9)	0.7071(9)	0.2848(7)	0.0230(10)
H1O1_1	1	−0.067(3)	0.3701(10)	0.1966(16)	0.029655
H1O1_2	1	0.356(3)	0.3691(15)	0.1886(16)	0.029655
H1O2_1	1	0.207(4)	0.2879(11)	0.0260(15)	0.020571
H1O2_2	1	0.742(4)	0.2911(14)	0.0103(16)	0.020571
H1O3_1	1	0.111(3)	−0.0429(11)	0.3571(18)	0.018694
H1O3_2	1	0.670(3)	−0.0367(16)	0.3887(13)	0.018694
H1O4_1	1	0.483(4)	0.8676(10)	0.1616(18)	0.018389
H1O4_2	1	0.977(4)	0.8684(13)	0.1956(16)	0.018389
H1O5_1	1	0.251(3)	0.240(3)	0.581(3)	0.030831
H1O5_2	1	0.845(3)	0.249(4)	0.596(2)	0.030831

2019). From all crystals measured, the four best 3D ED data sets were merged and treated together for the structure analysis, and two more were used to evaluate the unit-cell parameters. The result of the data reduction was a *hkl*-type file obtained from merging the four data sets with associated intensities and estimated standard deviations (R_{int}(obs/all) = 0.1703/0.3380). This file was used in the subsequent structure solution. For the refinement, considering the dynamical effects, the data sets were processed again separately to give *hkl*-type files where each ED frame is considered independent (Palatinus *et al.*, 2015a, 2015b). The structure was solved using *Superflip* (Palatinus and Chapuis, 2007; Palatinus, 2013) in *Jana2020* (Petříček *et al.*, 2020) and refined using *DYNGO* (Palatinus *et al.*, 2015b) and *Jana2020*. The data collection details are presented in Table 6.

Crystal-structure determination

Grandviewite is described in the triclinic supercell $a = 6.002(3)$ Å, $b = 10.54(3)$ Å, $c = 11.249(8)$ Å, $\alpha = 72.14(17)°$, $\beta = 81.56(60)°$, $\gamma = 86.10(79)°$ and $V = 669.8(12)$ $Å^3$ in space group $P\bar{1}$. The 3D ED data first revealed a strong subcell with parameters $a' = \frac{1}{2}ab = 10.54(3)$ Å, $c = 11.249(8)$ Å, $\alpha = 72.14(17)°$, $\beta = 81.56(60)°$, $\gamma = 86.10(79)°$ and $V' = \frac{1}{2}V = 334.9(12)$ $Å^3$ in space group $P\bar{1}$. The weaker supercell is obtained by doubling the a' parameters ($a = 6.002(3)$ Å). Depending on the crystal, supercell reflections are more or less weak and/or diffuse, showing that some crystals

are close to being disordered and some possess a more pronounced ordering. This work focuses on the description of the supercell. However, in order to shed light on the origin of the ordering and as only a few supercell reflections are observed (for $I \geq \sigma(I)$) with a rather diffuse profile, the structure was first determined in the subcell (see Fig. 6). Results obtained for the subcell are shown for comparison only, however we do not provide any additional details for the refinement. The superstructure has been solved *ab initio* from the merged data to increase the data completeness up to ~94.93% for a $\sin\theta/\lambda = 0.72$ $Å^{-1}$ resolution shell (see Table 6). The most important experimental parameters are listed in Table 6. The initial solution shows three Cu sites in pyramidal coordination, two Al sites in octahedral coordination, and two sites related to partially occupied SO_4. At this step, the solution in the subcell helped interpret the initial solution for the superstructure. In Fig. 6, the electrostatic potential map of the SO_4 chain is given in the subcell and the supercell. Though the copper- and the aluminium-centred polyhedra are not involved in the supercell ordering, the unique S and O7 sites from the subcell, which from the refinement result are half occupied, are clearly ordered in the supercell. In the subcell, the apical O8 site appears disordered between two positions (Fig. 6). This split, already visible from the structure solution, was later confirmed by the subcell refinement. In the supercell, the electrostatic potential corresponding to O8_1 and O8_2 is only visible close to the most occupied S site (labelled S1_2) and not visible at the $2\sigma[\Delta V(r)]$ level in the vicinity of the least occupied S1_1 site due to too low occupancy (Fig. 6). The comparison of the two solutions confirms the origin of the supercell due to the SO_4 ordering. The refinement of the supercell structure from 3D ED data has been carried out considering the dynamical effects (so-called 'dynamical refinement'). For well-crystallised samples, including the multiple scattering (dynamical effects) in the refinement of 3D ED a significant improvement in terms of structural parameters and *R*-factors (Palatinus *et al.*, 2015a, 2015b; Blum *et al.*, 2021) is obtained. Soft restraints on S–O and O–O distances were added to stabilise the refinement with the weak superstructure reflections. The sum of S1_1 and S1_2 occupancies is set to 1 in addition to all the oxygen sites involved in the SO_4 ordering: O7_1/O7_2, O8_1/O8_2 and O8b_1/O8b_2. The occupancy of oxygen atoms involved in the tetrahedral coordination of SO_4 is set to the occupancy of the corresponding S. After a few cycles, including non-hydrogen atoms, a residual electrostatic potential map (equivalent to a difference-Fourier map) was generated to reveal the hydrogen positions and their bond lengths (Table 7). Ten expected hydrogen sites are very visible (Fig. 7), with significant isosurface levels (Table 7). In the absence of the S1_1 or S2_2 atoms, O6_1 or O6_2 become H_2O molecules. However, the corresponding hydrogen sites forming H_2O are not visible due to their partial occupancies and are probably shadowed by the SO_4 disorder. All O–H distances were restrained to 1.03 Å according to the average value of the apparent O–H distances obtained from the difference-potential map (Table 7) (Clabbers *et al.*, 2019), and the isotropic displacement parameters of hydrogen atoms were set as riding with extension factor 1.5 (Palatinus *et al.*, 2017). The introduction of hydrogen in the refinement improved the *R*-factor by ~1% before the frame orientation optimisation. The last refinement steps led to $R(\text{obs})/wR(\text{obs}) = 0.1304/0.1316$ for 6401/31007 observed reflections with $I \geq 3\sigma(I)$ and 118 structural parameters (Table 6). Higher *R*-factors are obtained for superstructure reflections $h = 2n + 1$ ($R(\text{obs}) = 0.2386$ for 754 observed reflections)
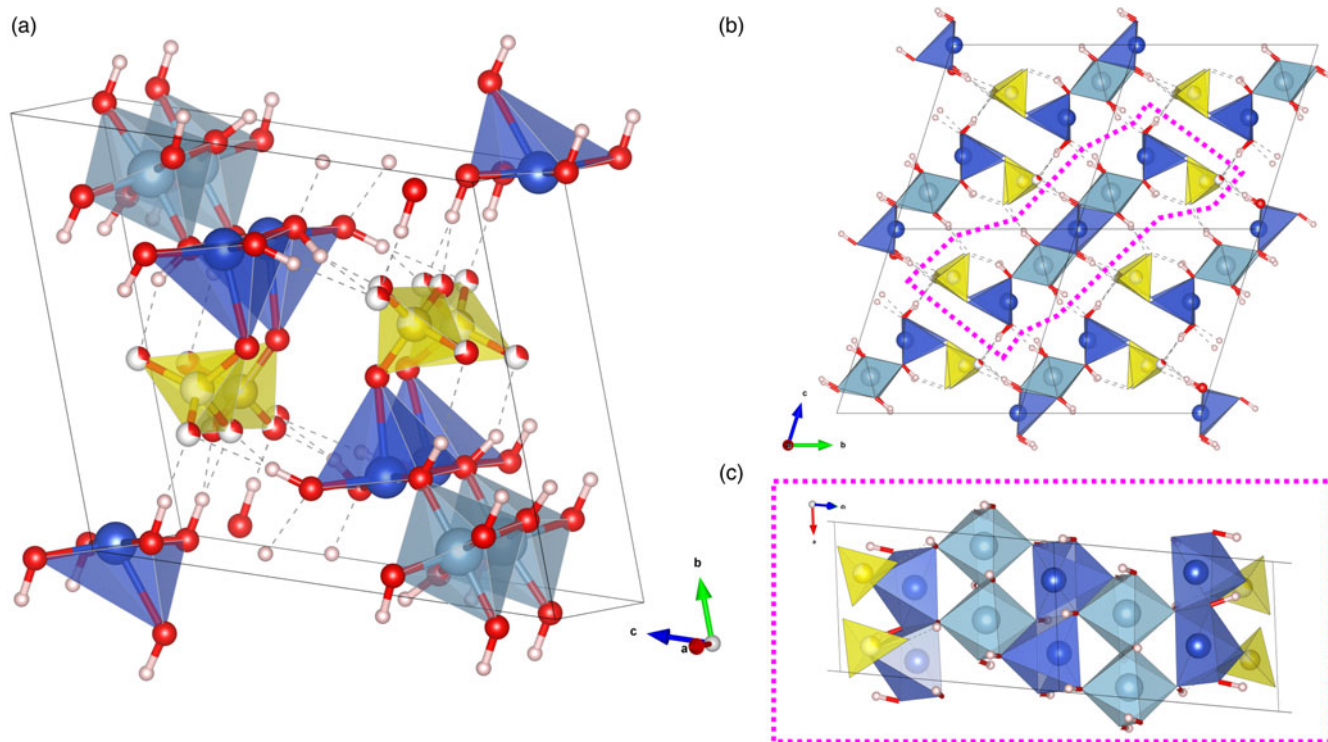
Fig. 8. (a) Grandviewite structure with partially occupied SO$_4$ chain. (b) (001) projection of grandviewite in four unit cells showing the fundamental building unit (FBU) (pink area) of the grandviewite structure linked to the other units by strong hydrogen bonds (dashed lines). (c) Topology of the FBU. SO$_4$, AlO$_6$ and CuO$_5$ polyhedra are represented in yellow, grey and blue, respectively.

coming from the supercell because they are weaker and less sharp than the reflections $h = 2n$ (R(obs) = 0.1222 for 5648 observed reflections) of the sub-structure. The refined formula is Cu$_3$Al$_2$(SO$_4$)(OH)$_{10}$(H$_2$O) for $Z = 2$, which is in line with results from the electron microprobe analyses. The refinement details are given in Table 6 and selected interatomic distances in Table 8. The positional and atomic displacement parameters are given in Table 9. Structural parameters are provided in the crystallographic information files which have been deposited with the Principal Editor of *Mineralogical Magazine* and are available as Supplementary material (see below).

Structure and topological description

The structure possesses three Cu sites in [4 + 2] and [4 + 1] coordinations, two Al sites in octahedral coordination, two partially occupied S sites in tetrahedral coordination, and sixteen oxygen atoms (two are disordered) involved in the polyhedral coordination. Ten hydrogen sites are responsible for ten hydroxyl groups in the structure (Fig. 8). Cu1 is in tetragonal bipyramidal coordination [4 + 2] and Cu2_1 and Cu2_2 are both in coordination [4 + 1] as tetragonal pyramids. All Cu1 are connected to each other through edges of the square plane of the bipyramid, thus
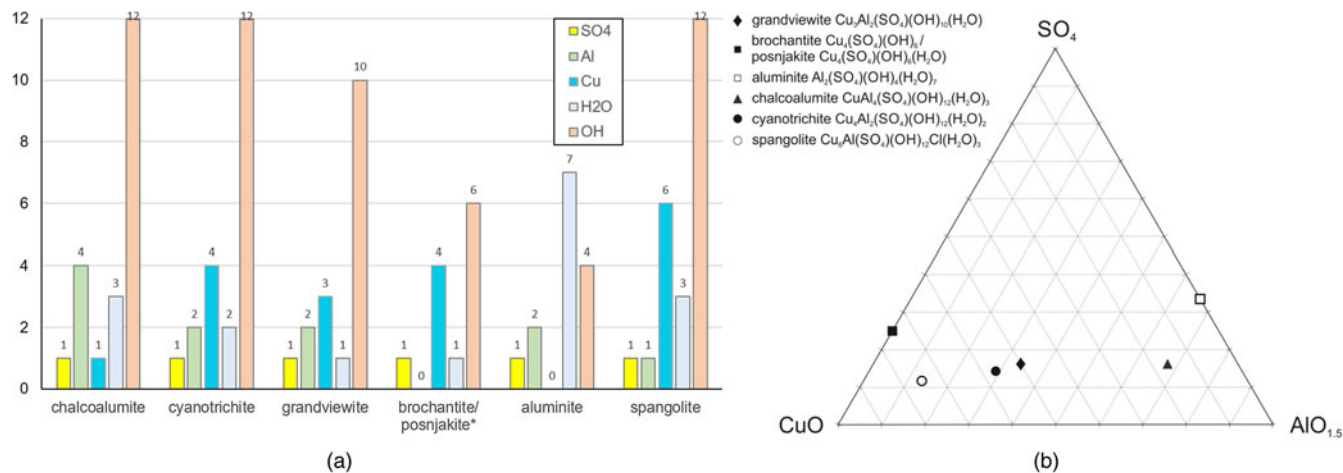

Fig. 9. (a) Graph with Cu, S Al, OH and H$_2$O contents in grandviewite and related minerals. * For brochantite/posnjakite, 1H$_2$O only corresponds to the amount in posnjakite. (b) Ternary diagram CuO–SO$_4$–AlO$_{1.5}$ (molar units) showing grandviewite compared to related minerals.

creating infinite chains along **a**. The same connectivity is observed between Cu2_1 and Cu2_2 and between the AlO_6 octahedra. In the (*b*,*c*) plane AlO_6–Cu1–AlO_6 form a flat slab that extends as an infinite chain along **a**, with Cu1-centred polyhedra connected via two edges on the top and two at the bottom with adjacent AlO_6 octahedra. Two chains of polyhedra centred by Cu2 (Cu2_1 and Cu2_2) are connected to the AlO_6 octahedra on both ends of the AlO_6–Cu1–AlO_6 slab through one vertex (O1_1 or O1_2). SO_4 tetrahedra form a disordered chain along **a**, alternated with occupancies of 30%/70% for S1_1/S1_2 as well as the terminal O7_1/O7_2 oxygen atoms and the O8 atoms forming the tetrahedra. They are connected to the Cu2-centered (Cu2_1 and Cu2_2) pyramids via the apical oxygen of the $^{[4+1]}CuO_5$ polyhedra and are otherwise stabilised by strong hydrogen bonds with surrounding units (Fig. 8b). All the polyhedra bonded via covalent bonds form a unit (pink outline in Fig. 8) with the formula $Cu_3Al_2(SO_4)(OH)_{10}$ that is extended infinitely along **a** and connected in the *b*,*c* plane via strong hydrogen bonds.

Grandviewite and related minerals

Grandviewite can be defined as part of the ternary system CuO–SO_4–$AlO_{1.5}$ with minerals such as chalcoalumite, cyanotrichite, spangolite, and some potential end-members such as brochantite, posnjakite, or aluminite (Fig. 9b). Among them, chalcoalumite and spangolite with the highest H_2O moieties (H_2O + OH) content (and, to some extent, chalcophyllite $Cu_{18}Al_2(AsO_4)_4(SO_4)_3(OH)_{24}\cdot36\ H_2O$) exhibit layered structures with (SO_4)-free copper-aluminium(-arsenate) layers and the $(SO_4)^{2-}$ tetrahedra located in the thick interlayer. For other reported minerals in the system, the structures are slab-based where the SO_4 tetrahedra are directly bonded to the Al–Cu units (except for the Cu-free end-member aluminite). For brochantite, representing a copper end-member, slabs of CuO_6 dimers are not independent and are interconnected via their vertices, and via the vertices of neighbouring SO_4. The concept of a fundamental building unit (FBU) appears for grandviewite and cyanotrichite where the connectivity between adjacent FBU is only ensured via strong hydrogen bonds (Fig. 8b and c). In terms of composition, cyanotrichite, $Cu_4Al_2(SO_4)(OH)_{12}(H_2O)_2$ (Mills *et al.*, 2015), is the closest known mineral to grandviewite, $Cu_3Al_2(SO_4)(OH)_{10}(H_2O)$ (Fig. 9a and b). As mentioned above, grandviewite was mistaken for a cyanotrichite-like mineral related to cyanotrichite and carbonatecyanotrichite because of their similar colour and rather close composition. Although distinct, their structures nevertheless possess similar features. Both minerals are built from parallel FBU, extending along the last direction to the infinite. The main differences lie (1) in the different FBU topology due to different Cu:Al ratio and, more importantly, (2) in the presence of a characteristic SO_4 ordering in grandviewite whereas SO_4 remains disordered in cyanotrichite.

Conclusion

New chemical and crystallographic data collected on grandviewite from the holotype (Grandview mine, Arizona) and additional specimens found at the Capillitas mine (Argentina) proved that both are identical within analytical uncertainties and this mineral is a hydrated copper-aluminium hydroxo-sulfate, having the significantly revised ideal formula $Cu_3Al_2(SO_4)(OH)_{10}\cdot H_2O$ ($Z = 2$) and a triclinic symmetry (space group $P\bar{1}$).

References

Bindi L., Putz H., Paar W.H. and Stanley C.J. (2017) Omariniite, $Cu_8Fe_2ZnGe_2S_{12}$, the germanium-analogue of stannoidite, a new mineral species from Capillitas, Argentina. *Mineralogical Magazine*, **81**, 1151–1159.

Blum T.B., Housset D., Clabbers M.T.B., Van Genderen E., Bacia-Verloop M., Zander U., McCarthy A.A., Schoehn G., Ling W.L. and Abrahams J.P. (2021) Statistically correcting dynamical electron scattering improves the refinement of protein nanocrystals, including charge refinement of coordinated metals. *Acta Crystallographica*, **D77**, 75–85.

Burnham C.W. (1962) Lattice constant refinement. *Carnegie Institute Washington Yearbook*, **61**, 132–135.

Čejka J., Sejkora J., Plášil J., Bahfenne S., Palmer S.J. and Frost R.L. (2011) A vibrational spectroscopic study of hydrated Fe^{3+} hydroxyl-sulfates; polymorphic minerals butlerite and parabutlerite. *Spectrochimica Acta*, **A79**, 1356–1363.

Clabbers M.T.B., Gruene T., van Genderen E. and Abrahams J.P. (2019) Reducing dynamical electron scattering reveals hydrogen atoms. *Acta Crystallographica*, **A75**, 82–93.

Colchester D.M., Klish D.R., Leverett P. and Williams P.A. (2008) Grandviewite, $Cu_3Al_9(SO_4)_2(OH)_{29}$, a new mineral from the Grandview Mine, Arizona, USA. *Australian Journal of Mineralogy*, **14**, 51–54.

Effenberger H., Lengauer C.L., Libowitzky E., Putz H. and Topa D. (2015) Lislkirchnerite, IMA 2015-064. CNMNC Newsletter No. 27, October 2015, page 1230. *Mineralogical Magazine*, **79**, 1229–1236.

Frost R.L., Sejkora J., Čejka J. and Keeffe E.C (2009) Raman spectroscopic study of the mixed anion sulphate–arsenate mineral parnauite $Cu_9[(OH)_{10}|SO_4|(AsO_4)_2]\cdot7H_2O$. *Journal of Raman Spectroscopy*, **40**, 1546–1550.

Gemmi M. and Lanza A.E. (2019) 3D electron diffraction techniques. *Acta Crystallographica*, **B75**, 495–504.

Gemmi M., Mugnaioli E., Gorelik T.E., Kolb U., Palatinus L., Boullay P., Hovmöller S. and Abrahams J.P. (2019) 3D electron diffraction: The nanocrystallography revolution. *ACS Central Science*, **5**, 1315–1329.

Kolb U., Gorelik T., Kübel C., Otten M.T. and Hubert D. (2007) Towards automated diffraction tomography: Part I-Data acquisition. *Ultramicroscopy*, **107**, 507–513.

Kolb U., Gorelik T. and Otten M.T. (2008) Towards automated diffraction tomography. Part II-Cell parameter determination. *Ultramicroscopy*, **108**, 763–772.

Kraus W. and Nolze G. (1996) POWDER CELL – a program for the representation and manipulation of crystal structures and calculation of the resulting X-ray powder patterns. *Journal of Applied Crystallography*, **29**, 301–303.

Mandarino J.A. (1981) The Gladstone-Dale relationship: Part IV. The compatibility concept and its application. *The Canadian Mineralogist*, **19**, 441–450.

Márquez-Zavalía M.F. (1999) El Yacimiento Capillitas, Catamarca. Pp. 1643–1652 in: *Recursos Minerales de la República Argentina* (E.O. Zappettini, editor). Volume 35. SEGEMAR, Buenos Aires, Argentina [in Spanish].

Márquez-Zavalía M.F. (2006) El extremo rico en As de la serie Jordanita-Geocronita de Capillitas, Catamarca, Argentina. *Revista de la Asociación Geológica Argentina*, **61**, 231–235 [in Spanish].

Márquez-Zavalía M.F. and Craig J.R. (2004) Telluride and precious metal mineralization at Mina Capillitas, Northwestern Argentina. *Neues Jahrbuch für Mineralogie – Monatshefte*, **2004**, 176–192.

Márquez-Zavalía M.F. and Heinrich C.A. (2016) Fluid evolution in a volcanic-hosted epithermal carbonate–base-metal–gold vein system: Alto de la Blenda, Farallón Negro, Argentina. *Mineralium Deposita*, **51**, 873–902.

Márquez-Zavalía M.F. and Pedregosa J.C. (1994) Cianotriquita y carbonatocianotriquita de mina Capillitas, Catamarca. *Revista de la Asociación Geológica Argentina*, **49**, 353–358.

Márquez-Zavalía M.F., Craig J.R. and Solberg T.N. (1999) Duranusite, product of realgar alteration, Mina Capillitas, Argentina. *The Canadian Mineralogist*, **37**, 1255–1259.

Márquez-Zavalía M.F., Galliski M.A., Drábek M., Vymazalová A., Watanabe Y., Murakami H. and Bernhardt H.-J. (2014) Ishiharaite, (Cu,Ga,Fe,In,Zn)S, a new mineral from Capillitas mine, northwestern Argentina. *The Canadian Mineralogist*, **52**, 969–980.

Márquez-Zavalía M.F., Vymazalová A., Galliski M.A., Watanabe Y. and Murakami H. (2020) Indium-bearing paragenesis from the Nueva Esperanza and Restauradora veins, Capillitas mine, Argentina. *Journal of Geosciences*, **65**, 95–109.

Mills S.J., Christy A.G., Colombo F. and Price J.R. (2015) The crystal structure of cyanotrichite. *Mineralogical Magazine*, **79**, 321–335.

Miyawaki R., Hatert F., Pasero M. and Mills S.J. (2022) Newsletter 65. *Mineralogical Magazine*, **86**, 354–358, https://doi.org/10.1180/mgm.2022.14.

Mugnaioli E., Gorelik T. and Kolb U. (2009) "Ab initio" structure solution from electron diffraction data obtained by a combination of automated diffraction tomography and precession technique. *Ultramicroscopy*, **109**, 758–765.

Mugnaioli E., Lanza A.E., Bortolozzi G., Righi L., Merlini M., Cappello V., Marini L., Athanassiou A. and Gemmi M. (2020) Electron diffraction on flash-frozen cowlesite reveals the structure of the first two-dimensional natural zeolite. *ACS Central Science*, **6**, 1578–1586.

Myneni S.C. (2000) X-ray and vibrational spectroscopy of sulfate in earth materials. Pp. 113–172 in: *Sulfate Minerals: Crystallography, Geochemistry, and Environmental Significance* (C.N. Alpers, J.L. Jambor, and D.K. Nordstrom, editors). Reviews in Mineralogy and Geochemistry, **40**. Mineralogical Society of America and the Geochemical Society, Washington DC.

Nakamoto K. (2009) *Infrared and Raman Spectra of Inorganic and Coordination Compounds, Part A, Theory and Applications In Inorganic Chemistry*. 6th ed. John Wiley & Sons, Inc., Hoboken, New Jersey, USA, 419 pp.

Ondruš P. (1993) A computer program for analysis of X-ray powder diffraction patterns. *Materials Science Forum, EPDIC-2, Enchede*, **133–136**, 297–300.

Paar W.H., Roberts A.C., Berlepsch P., Armbruster T., Topa D. and Zagler G. (2004) Putzite, $(Cu_{4.7}Ag_{3.3})_8GeS_6$, a new mineral species from Capillitas, Catamarca, Argentina: description and crystal structure. *The Canadian Mineralogist*, **42**, 1757–1769.

Palatinus L. (2013) The charge-flipping algorithm in crystallography. *Acta Crystallographica*, **B69**, 1–16.

Palatinus L. and Chapuis G. (2007) SUPERFLIP – A computer program for the solution of crystal structures by charge flipping in arbitrary dimensions. *Journal of Applied Crystallography*, **40**, 786–790.

Palatinus L., Corrêa C.A., Steciuk G., Jacob D., Roussel P., Boullay P., Klementová M., Gemmi M., Kopeček J., Domeneghetti M.C., Cámara F. and Petříček V. (2015a) Structure refinement using precession electron diffraction tomography and dynamical diffraction: tests on experimental data. *Acta Crystallographica*, **B71**, 740–751.

Palatinus L., Petříček V. and Correâ C.A. (2015b) Structure refinement using precession electron diffraction tomography and dynamical diffraction: Theory and implementation. *Acta Crystallographica*, **A71**, 235–244.

Palatinus L., Brázda P., Boullay P., Perez O., Klementová M., Petit S., Eigner V., Zaarour M. and Mintova S. (2017) Hydrogen positions in single nanocrystals revealed by electron diffraction. *Science*, **355**, 166–169.

Palatinus L., Brázda P., Jelínek M., Hrdá J., Steciuk G. and Klementová M. (2019) Specifics of the data processing of precession electron diffraction tomography data and their implementation in the program PETS2.0. *Acta Crystallographica*, **B75**, 512–522.

Petříček V., Dušek M., and Palatinus L. (2020) *Crystallographic computing system Jana2020*. Institute of Physics of the ASCR, Prague, Czech Republic.

Plana-Ruiz S., Portillo J., Estradé S., Peiró F., Nicolopoulos S. and Kolb U. (2018) Quasi-parallel precession diffraction: Alignment method for scanning transmission electron microscopes. *Ultramicroscopy*, **193**, 39–51.

Pouchou J.L. and Pichoir F. (1985) "PAP" (φρZ) procedure for improved quantitative microanalysis. Pp. 104–106 in: *Microbeam Analysis* (J. T. Armstrong, editor). San Francisco Press, San Francisco, USA.

Putz H., Paar W.H., Topa D., Makovicky E. and Roberts A.C. (2006) Catamarcaite, Cu_6GeWS_8, a new species of germanium–tungsten sulfide from Capillitas, Catamarca, Argentina: description, paragenesis and crystal structure. *The Canadian Mineralogist*, **44**, 1481–1497.

Putz H., Paar W.H. and Topa D. (2009) A contribution to the knowledge of the mineralization at mina Capillitas, Catamarca. *Revista de la Asociación Geológica Argentina*, **64**, 514–524.

Steciuk G., Majzlan J. and Plášil J. (2021a) Hydrogen disorder in kaatialaite Fe$(AsO_2(OH)_2)\cdot5H_2O$ from Jáchymov, Czech Republic: determination from low temperature 3D electron diffraction. *International Union of Crystallography Journal*, **8**, 2052–2525.

Steciuk G., Sejkora J., Čejka J., Plášil J. and Hloušek J. (2021b) Krupičkaite, $Cu_6[AsO_3(OH)]_6\cdot8H_2O$, a new copper arsenate mineral from Jáchymov (Czech Republic). *Journal of Geosciences*, **66**, 37–50.

Vincent R. and Midgley P.A. (1994) Double conical beam-rocking system for measurement of integrated electron diffraction intensities. *Ultramicroscopy*, **53**, 271–282.

Viramonte J.G., Galliski M.A., Araña Saavedra V., Aparicio A., García Cacho L. and Martín Escorza C. (1984) El finivulcanismo básico de la depresión de Arizaro, provincia de Salta. *IX Congreso Geológico Argentino, Actas*, III, 234–251 [in Spanish].